CHALMERS
UNIVERSITY OF TECHNOLOGY

Investigation of the strengthening mechanism in 316L stainless steel produced with laser powder bed fusion

Materials Science & Engineering A 822 (2021) 141699

Contents lists available at ScienceDirect

Materials Science & Engineering A

journal homepage: www.elsevier.com/locate/msea

Investigation of the strengthening mechanism in 316L stainless steel produced with laser powder bed fusion

D. Riabov [*,1], A. Leicht [1], J. Ahlström, E. Hryha

Chalmers University of Technology, Department of Industrial and Material Science, Sweden

ARTICLE INFO

Keywords:
Additive manufacturing
Stainless steel
Microstructure
Texture
Strengthening mechanism
Mechanical properties

ABSTRACT

Of the many benefits of the additive manufacturing process, laser powder bed fusion (L-PBF) has specifically been shown to produce hierarchical microstructures that circumvent the common strength-ductility trade-off. Typically, high strength materials have limited ductility, and vice versa. The L-PBF microstructure, consisting of fine cells, is formed during the rapid solidification of the laser powder bed fusion process. The cell boundaries are often characterized by the segregation of alloying elements and a dislocation network. While there are a number of works describing the strengthening mechanisms in L-PBF-produced 316L, there are still some gaps in understanding the effect of stress-relief and annealing at various annealing temperatures (400, 800 and 1200 °C) on the plastic strain accumulation during deformation. In this study, the authors evaluated strain partitioning using electron backscatter diffraction and kernel average misorientation maps. The results show strain partitioning to be dependent on both the annealing temperature and the pre-straining of samples. Further, the results indicated that the dislocation structure was stable until 400 °C, whereas at 800 °C strain was no longer detected at the cell boundaries. Similarly, after the heat treatment at 800 °C, elemental segregation at the cell walls was no longer detectable. Upon straining, the boundaries of as-built and annealed samples at 400 and 800 °C registered accumulation of additional strain as compared to the unstrained states. The results demonstrate that even a weak array of dislocations along the cell walls can successfully pin dislocations, albeit at a reduced capability relative to the co-existent dislocation and segregate structures found in microstructures of the as-built and annealed samples at 400 °C.

1. Introduction

The stainless steel alloy 316L is frequently used in energy, automotive and medical industries because of its excellent corrosion properties, formability and high strain-hardening rates. However, the yield strength of a conventional 316L in its annealed state is rather low, ranging between 150 and 300 MPa. This limits its use in structural or load-bearing applications where higher yield strength is typically required. One method to increase the strength of 316L is through cold rolling or other forms of deformation, where the heavy deformation produces an array of dislocation networks that effectively harden the material. Another approach is to anneal the heavily deformed material so that grain refinement takes place during recrystallization, forming fine or possibly ultra-fine grains (UFG); the process hence increases the strength according to the Hall-Petch relationship, which describes the relationship between grain size and material strength. The topic of UFG and nano-grained materials has been heavily researched, and a common drawback of these materials is that they lose their ductility [1–8]. This phenomenon is also known as the strength-ductility trade-off.

Recent developments within the field of additive manufacturing have shown the possibility of producing microstructural features that also drastically improve the strength-ductility trade-off, specifically when using laser-powder bed fusion (L-PBF) technology [9–11]. Numerous investigations have shown that processing stainless steel 316L via L-PBF creates a hierarchical microstructure consisting of large elongated grains, melt pool boundaries, distinct cellular structures and submicron precipitates [9,10,12–16]. The cellular structures are considered to be the main reason for the improved properties [9,12,15], and are believed to form due to extensive thermo-mechanical cycling during the build process [17–19]. Furthermore, the self-arranging dislocation network was proposed to be the driving force for the elemental segregation commonly found in L-PBF processed 316L

* Corresponding author.
E-mail address: riabov@chalmers.se (D. Riabov).
[1] These authors contributed equally to this work.

https://doi.org/10.1016/j.msea.2021.141699
Received 4 May 2021; Received in revised form 29 June 2021; Accepted 3 July 2021
Available online 4 July 2021

materials. Hence, the cell boundaries exhibit a complex dislocation network together with enrichment of Cr and Mo [9–11,18]. It seems that both the segregation and the dislocations at the cell boundaries provide a soft dislocation pinning effect [11], hence increasing the strength while maintaining high ductility. Furthermore, Wang et al. [9] found significant formation of twin boundaries upon deformation, hence creating multiple interfaces where dislocation interactions are possible. Liu et al. [11] further investigated twin formation, finding that twins formed as dislocations dissociated into partials when traveling through cell walls.

While the cell structure has been identified as a strength promoter in the as-built state, there is still a gap in understanding how this structure develops during annealing. More particularly, it is unclear how different temperatures during the annealing process affect the strengthening mechanism. Furthermore, heat treatment of L-PBF processed materials has been shown to reduce the strength of the materials, which is believed to be due to the gradual removal of the cell structure [20,21]. Studies have also shown that the cellular network completely anneals out between temperatures of 900 and 1100 °C [16,22] due to both dislocation recovery and redistribution of elemental segregates [23,24]. A recent study investigated the evolution of the dislocation density as a function of annealing temperatures; the authors found that dislocation recovery mechanisms occurs at 700 °C [23]. The same study also distinguished between statistically stored dislocations (SSD) and geometrically necessary dislocations (GND) and found that SSDs rapidly anneal out, while GNDs are stable at higher temperatures. Hence, at intermediate annealing temperatures (below 900 °C), researchers believe some of the segregated elements will still be trapped, yet the dislocation tangles begin to recover. This would render a cell structure consisting primarily of segregated elements. This begs the following question: can the segregation network alone hinder dislocation movement, or are both necessary for improved strength properties?

To answer this question, the current work investigates the influence of heat treatment temperatures on the stability and characteristics of the cell boundaries. It also examines how heat treatment temperature influences the mechanical response of the material. Furthermore, the authors investigated the ability of the cell boundaries to accommodate strain as a function of the heat treatment temperature by comparing strained to unstrained samples using electron backscattered diffraction.

2. Materials and methods

An inert-gas-atomized 316L powder with a sieve fraction of 20–53 μm and an EOS M290 machine were used to produce the samples for this study. The samples were printed using a 20 μm layer thickness and standard process parameters developed by EOS GmbH for 316L stainless steel (316L Surface M291 version 1.10). The machine was equipped with a Yb-fiber laser with a maximum power of 400 W, had a base plate of 250 × 250 mm^2 and a maximum build height of 325 mm. The builds were conducted under argon atmosphere with an oxygen content below 0.1%. Tensile test bars were produced with the dimensions provided in Fig. 1, which are in accordance with the ASTM E8/E8M-15a standard.

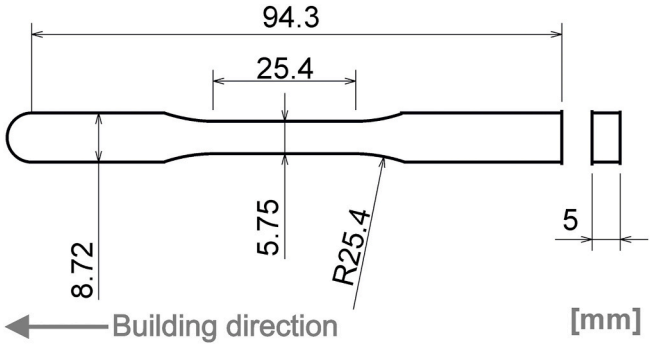

Fig. 1. Dimensions of the tensile test bar and the building direction.

The chemical compositions were obtained by using inductively coupled plasma-optical emission spectrometry (SPECTRO ARCOS), combustion gas analysis for carbon and sulfur (LECO CS844) and hot fusion analysis for the oxygen and nitrogen using a LECO ON836 instrument.

The samples used in this study were investigated in as-built and heat-treated conditions. The samples were heat-treated at 400 °C, 800 °C and 1200 °C for 1h in a batch furnace under argon atmosphere followed by air cooling to achieve fast cooling rates. Fig. 2 shows the heat treatment process diagram.

Tensile tests were conducted at room temperature with a Zwick Z100 machine using the recommended strain rates provided by ISO 6892–1:2019 (0.0002 s^{-1} up to the yield stress, thereafter 0.0067 s^{-1}). For each condition, 15 individual samples were tested to ensure the necessary statistics would be obtained. In addition, each condition was pre-strained to 20% at a strain rate of 0.00167 s^{-1} to study the deformed microstructure. The area reduction at the fracture surface was evaluated using the following equation:(1)

$$Area\ reduction = \frac{A_0 - A_f}{A_0}$$

Here, A_0 is the original cross section while A_f is the cross section after fracture. A_f was measured by capturing the fracture surface using a Zeiss stereo microscope, and measurements of the area were made using Zeiss Axiovision software.

One sample from each condition was used for microstructural characterization. A cross-section obtained from the middle of the gauge length was mounted in conductive resin to examine the microstructure along and transverse to the building direction. The samples were prepared following Struers recommendations for stainless steel. The samples were plane ground using 500 grit SiC paper followed by fine grinding using a 9 μm diamond suspension. Polishing was done using 3 and 1 μm diamond suspensions followed by a final polish using colloidal silica for a duration of 20 min. The microstructure was revealed using electro-chemical etching, using a 3V potential in a water-based 10% oxalic acid solution. The microstructure was analyzed with a field emission gun scanning electron microscope (SEM – Leo Gemini 1550 SEM). Grain orientation and texture were determined by means of the electron backscattered diffraction (EBSD) technique using a Nordlys II detector (Oxford Instruments) and HKL Channel 5 data processing software. All measurements were performed with an accelerating voltage of 20 kV and the step size was dependent on the magnification. The orientation maps depict high-angle grain boundaries using black solid lines, which are defined by a misorientation greater than 15°. The

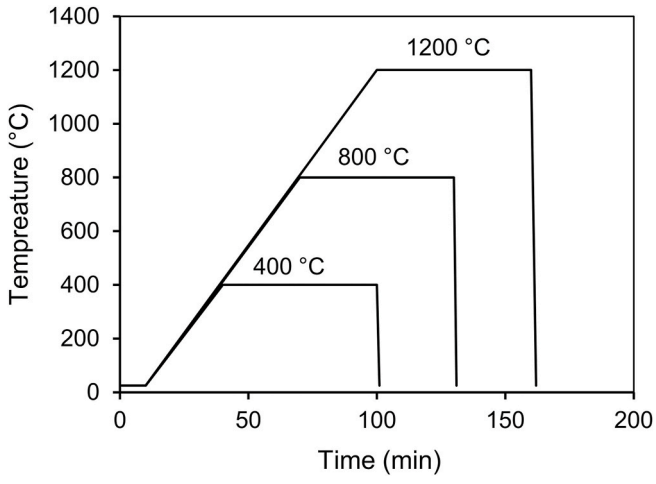

Fig. 2. Heat treatment process diagram.

kernel average misorientation (KAM) maps were calculated with the nearest neighbor pixels having a 2° misorientation threshold (to avoid the influence of grain boundaries). Cell and grain size determination was performed according to the lineal intercept method as described in the ASTM E112-13 standard. For the cell size counting, 10 micrographs were used per condition, rendering roughly 2500 counted cells per sample. For the grain size, three EBSD maps were used to evaluate the cross sections parallel to the building direction in all studied conditions, for the sample heat-treated at 1200 °C perpendicular cross sections were similarly evaluated. Transmission electron microscopy (TEM) was performed with a FEI Tecnai T20, equipped with EDX and HAADF detectors and operated at 200 kV. For HAADF imaging, a camera length of 100 mm was used. Thin foils were prepared by mechanically thinning samples down to roughly 100 μm followed by electrolytic twin-jet polishing until perforation using a 10% perchloric solution that was cooled to −30 °C.

3. Results

3.1. Chemical composition

Table 1 presents the chemical composition of the feedstock powder together with the analysis of oxygen and nitrogen in the as-built and heat-treated states in Table 2. As Table 2 shows, the as-built sample and the sample that was heat-treated at 400 °C had an oxygen content of about 0.045%. When the samples are heat-treated at 800 °C, a slight oxygen uptake of approximately 0.005 weight percent (wt.%) occurred, while the heat treatment at 1200 °C led to a higher rate of oxygen uptake (approximately 0.035 wt.%) compared to the as-built sample. The higher temperatures promoted the dissolution and diffusion of oxygen into the 316L stainless steel sample. The nitrogen content, however, seemed to be stable over all temperatures.

3.2. Microstructure characterization

Fig. 3 sets out high magnification SEM images of the samples in as-built and heat-treated conditions. The fine cellular structure together with melt pool boundaries were clearly visible in the as-built (Fig. 3a and b) and heat-treated at 400 °C (Fig. 3c and d) samples. As the heat treatment temperature was increased to 800 °C, the cells and melt pool boundaries began to dissolve but could still be discerned, as shown in Fig. 3e and f. After the heat treatment at 1200 °C, the melt pool boundaries and cells were no longer observed; instead, only macro-sized grains together with some annealing twins were perceived (see Fig. 3g and h).

Next, Table 3 presents the cell size. The values remained constant when comparing the as-built state with the sample that was heat-treated at 400 °C. In contrast, apparent measurements of the sample heat-treated at 800 °C indicated cells that were approximately 30% larger. However, at this temperature, the cell walls had become diffuse; as a result, the determination was not very accurate (as indicated by the sudden increase in scatter). For the sample heat-treated at 1200 °C, it was not possible to determine the cell size as the cells were completely dissolved.

Fig. 4a and b presents EBSD orientation maps of the as-built sample acquired from cross-sections that were both parallel (Fig. 4a) and perpendicular (Fig. 4b) to the building direction. The EBSD orientation map of the as-built sample that was parallel with the building direction consisted of large, elongated grains that grew epitaxially along the building direction over several melt pool boundaries (Fig. 4a). In contrast, the EBSD orientation map of the sample that was perpendicular to the building direction (Fig. 4b) had more equiaxed shaped grains. The samples also had a strong <101> crystallographic orientation, indicated by the majority of green-colored grains in Fig. 4. This was also seen in the high intensity of the <101> orientation in the respective inverse pole figures. No significant difference in the preferential orientation was observed between the as-built samples and the heat-treated samples (see supplemented Figure S1). However, a tendency towards an increased grain size in samples that had been heat-treated at 1200 °C was observed. The grain size of the samples is summarized in Table 4. It should be noted that within the microstructure of the sample heat-treated at 1200 °C, annealing twins were evident and were disregarded during the counting. Fig. 5 presents KAM maps acquired from the as-built sample and the sample heat-treated at 1200 °C. The as-built sample exhibited a high amount of local misorientation, evidenced by the predominance of green and yellow colors, which indicates an overall higher stress state. In contrast, the sample heat-treated at 1200 °C showed areas that had been partially recrystallized, denoted by the blue color in Fig. 5b. The blue areas exhibited low levels of misorientation, and hence can be considered stress-free. The findings from the KAM maps confirmed the observations that the heat treatment at 1200 °C had caused a partial recrystallization with grain growth as a consequence. No recrystallization was observed in the samples heat-treated at 400 °C and 800 °C, as shown in supplementary Figure S2.

The as-built sample and the sample heat-treated at 800 °C were investigated further using TEM, with the results presented in Fig. 6 and Fig. 7, respectively. The as-built condition shows clearly defined cells with dense dislocation tangles at the cell walls. Moreover, EDX measurements across the cell walls showed slight elemental segregation of Cr and Mo, something that was no longer detected across the faint boundaries in the sample that had been heat-treated at 800 °C. The EDX quantification was a bit noisy; the same plots using integrated counts are shown in supplementary Figure S5. Additionally, the cell walls in Fig. 7 did not contain thick dislocation tangles. Instead, only a few dislocations were observed on the cell walls. Also seen in Fig. 7b are spherical oxides that appear both with a dark and a light contrast. These oxides originate from the powder surface oxides that are carried over into the built component during L-PBF processing. The amount and composition is determined by the powder surface oxide state and processing atmosphere [22,25,26]. During powder melting, these surface oxides spheroidize and the convective currents in the melt pool ensures a fine distribution in the matrix.

To investigate the influence of cell boundaries on stress-strain partitioning during deformation, samples were strained to 20%. Kernel average misorientation maps were acquired and analyzed, hence providing a quantification of the average misorientation. In general, strain accumulation creates the EBSD misorientation, which could be translated to the presence and arrangement of dislocations. Fig. 8 and Fig. 9 present the KAM maps and the misorientation distribution plots of the samples in unstrained and 20%-strained conditions. The maps are

Table 2
Oxygen and nitrogen analysis of the as-built and heat-treated specimens in weight percent (wt.%).

	Oxygen	Nitrogen
As-built	0.046	0.075
Heat-treated at 400 °C	0.045	0.067
Heat-treated at 800 °C	0.050	0.072
Heat-treated at 1200 °C	0.082	0.082

Table 1
The chemical composition of the powder in weight percent (wt.%).

Elements	C	O	N	S	Si	Cr	Ni	Mn	Mo	P	Fe
Powder	0.02	0.079	0.11	0.006	0.6	17.0	12.7	1.5	2.5	0.02	Bal.

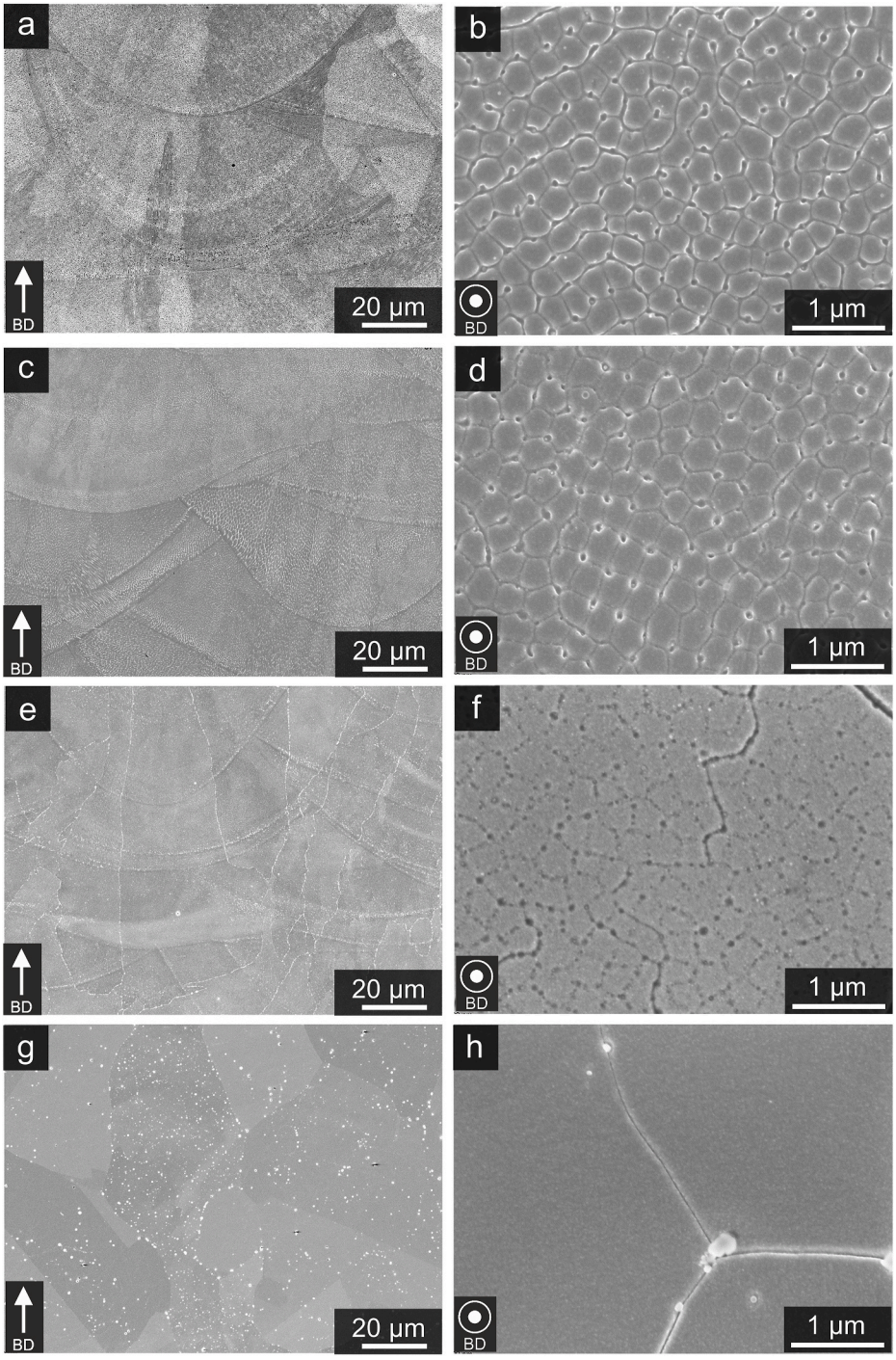

Fig. 3. SEM images taken from samples in the as-built (a, b), 400 °C (c, d), 800 °C (e, f) and 1200 °C (g, h) conditions.

Table 3
The average cell size with a 95% confidence interval of as-built and heat-treated samples (measured on cross sections perpendicular to the building direction).

Sample	Average cell size
As-built	0.43 ± 0.02 μm
Heat-treated at 400 °C	0.42 ± 0.05 μm
Heat-treated at 800 °C	0.64 ± 0.11 μm
Heat-treated at 1200 °C	N/A

presented using a rainbow color scale, where the blue color represents a 0° misorientation and red represents a 2° misorientation. It should be noted that in order to obtain strain information in the cell boundaries, the KAM maps presented in Fig. 8 utilize a much smaller step size compared to the KAM maps presented in Fig. 5a. A larger step size means that local strain accumulation of individual cells is absent or smeared out, and a dissimilar appearance is therefore seen when comparing Fig. 5a and the unstrained as-built sample in Fig. 8.

The samples showed a heterogeneous distribution of misorientation, namely accumulation in the cell boundaries with limited misorientation inside the cells, which is apparent in the KAM maps (Fig. 8). By straining the samples, the strain accumulation in the cell boundaries increased,

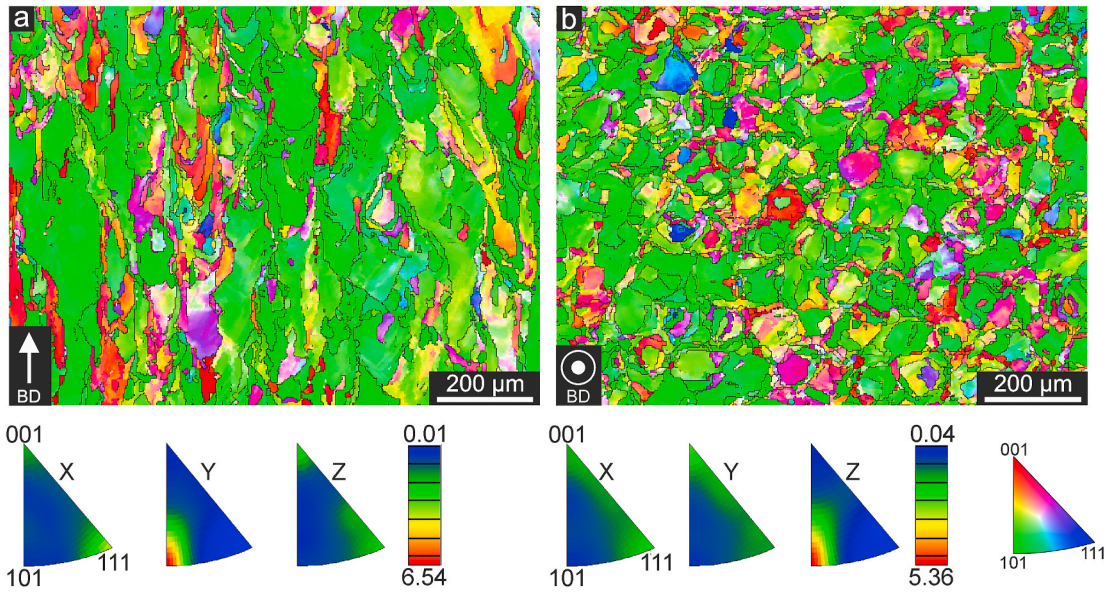

Fig. 4. EBSD orientation maps obtained of the as-built sample with the building direction parallel (a) and perpendicular (b) to the cross-section.

Table 4
The average grain size of the as-built and heat-treated samples, perpendicular and parallel to the building direction. The parallel cross sections include standard deviations.

	Perpendicular	Parallel
As-built	20 μm	27 ± 3 μm
Heat-treated at 400 °C	21 μm	27 ± 3 μm
Heat-treated at 800 °C	20 μm	29 ± 1 μm
Heat-treated at 1200 °C	38 μm ± 3 μm	38 ± 3 μm

indicating that dislocations are pinned in the cell boundaries. Note that the strain accumulation is less evident in the samples that were heat-treated at 400 °C and 800 °C. In the samples heat-treated at 1200 °C, no pronounced accumulation was found because the cells had been removed. It should also be noted that the melt pool boundaries did not accumulate any strain, as can be seen in supplementary Figure S3.

The misorientation distribution plots provided in Fig. 9 show that increasing the annealing temperature shifts the distribution peak to lower misorientation angles, making the peaks become narrower. This is also revealed by the full width at half maximum values presented in Table 5. The applied strain had two main effects on the misorientation distribution. First, the peak position was moved to higher values; for example, the peak position of the strained and unstrained 1200 °C heat-treated samples moved from 0.135 to 0.215, respectively. This movement was gradually reduced as the temperature decreased, whereas no shift was observed in the as-built sample. Secondly, the peaks broadened for all the strained samples, also seen in Table 5.

Additionally, the cell size was measured again after deformation in order to determine whether strain predominantly accumulates within the cells. This is because, in that scenario, the cells would change their aspect ratio as they stretch. Table 6 shows the results from these measurements; the 800 and 1200 °C samples were not included here due to a large spread or lack of values. Based on the measurements, no significant difference could be detected between the undeformed and deformed cells.

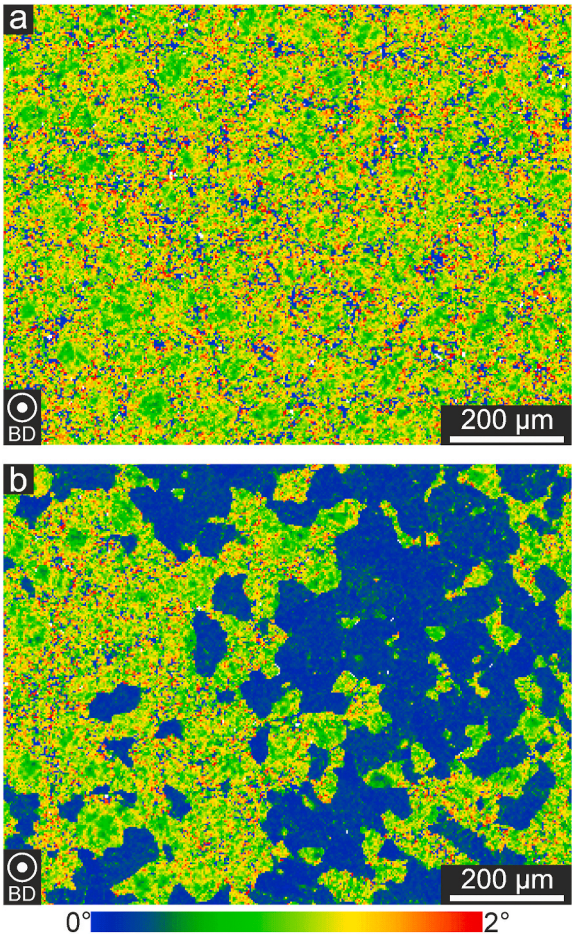

Fig. 5. KAM maps of (a) as-built and (b) heat-treated at 1200 °C samples.

3.3. Mechanical properties

Fig. 10a shows representative tensile test curves of the samples in the as-built and heat-treated conditions. Fig. 10b provides the average values of the tensile properties obtained from 15 individual samples of each condition. The yield strength was found to be the highest for the as-built samples and decreased as heat-treating temperatures increased. The scatter of the yield strength of the as-built samples and the samples heat-treated at 400 °C was high compared to the other two conditions. This was, however, expected as the derivative of the curve at the yield

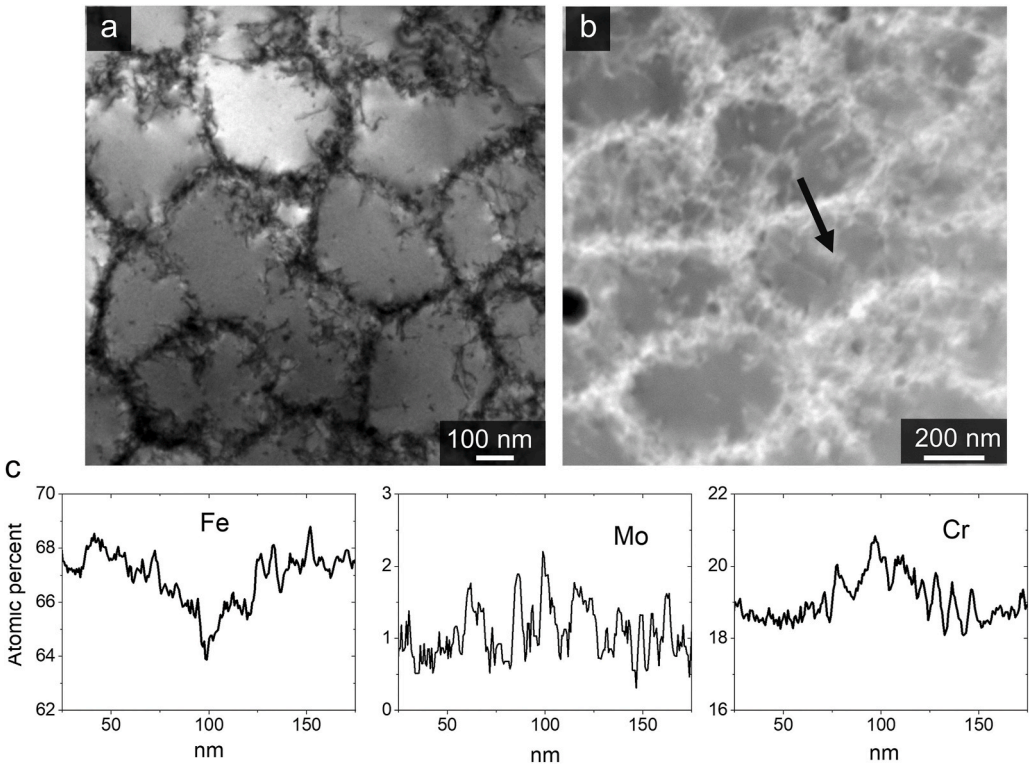

Fig. 6. TEM micrographs of the as-built sample with the building direction perpendicular to the cross section; a) bright field, b) STEM HAADF with the corresponding EDX line scan shown by the arrow, c) results.

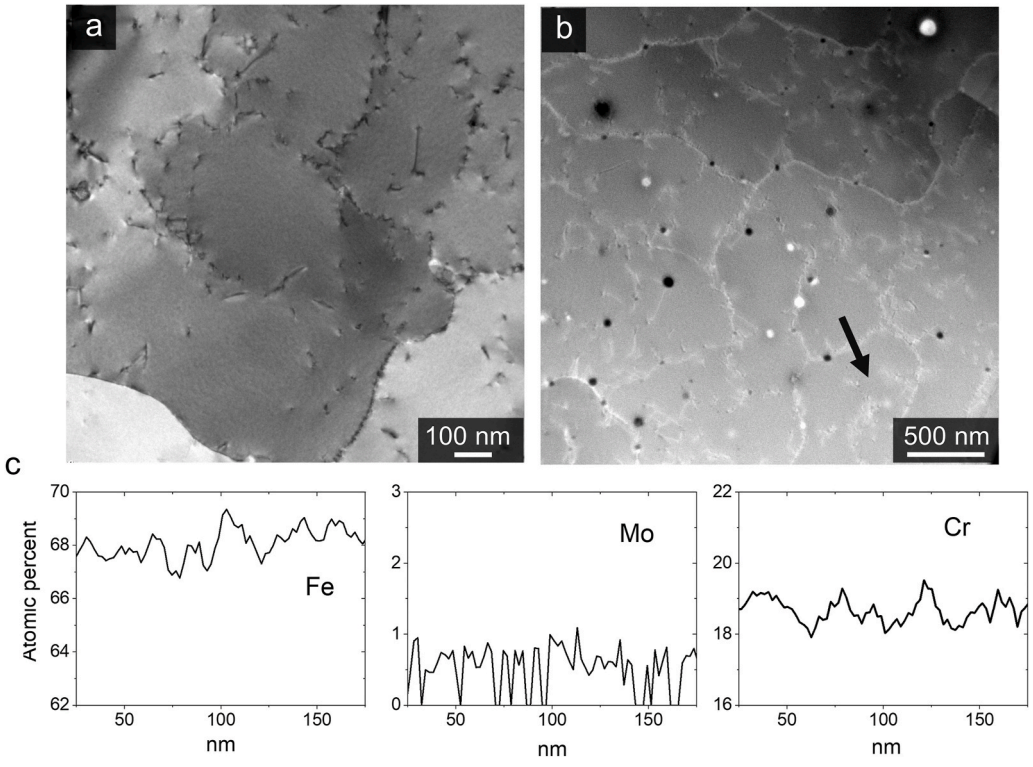

Fig. 7. TEM micrographs of the sample heat-treated at 800 °C with the building direction perpendicular to the cross section; a) bright field, b) STEM HAADF with the corresponding EDX line scan shown by the arrow, and c) results.

point ($d\sigma/d\varepsilon$ at R_p) was much higher for these conditions. Consequently, determining yield strength with the $R_{p0.2}$ off-set method automatically generates more scatter. The as-built samples exhibited slightly higher tensile strength and comparable total elongation to fracture (or ductility) compared to the sample heat-treated at 400 °C. As the heat treatment temperature was increased further, a significant decrease in

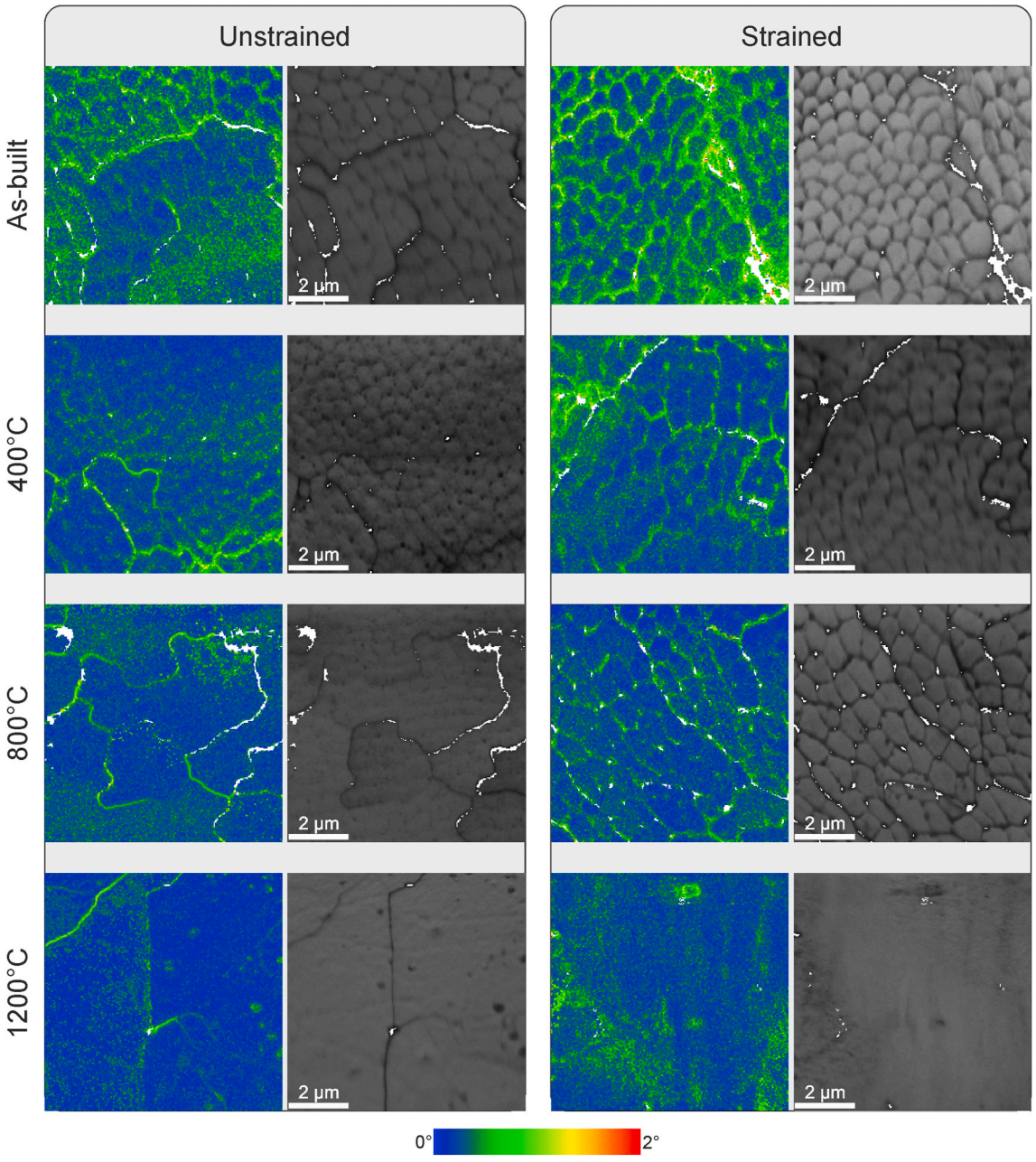

Fig. 8. KAM and band contrast images of the as-built and heat-treated samples in unstrained (left) and strained (right) samples.

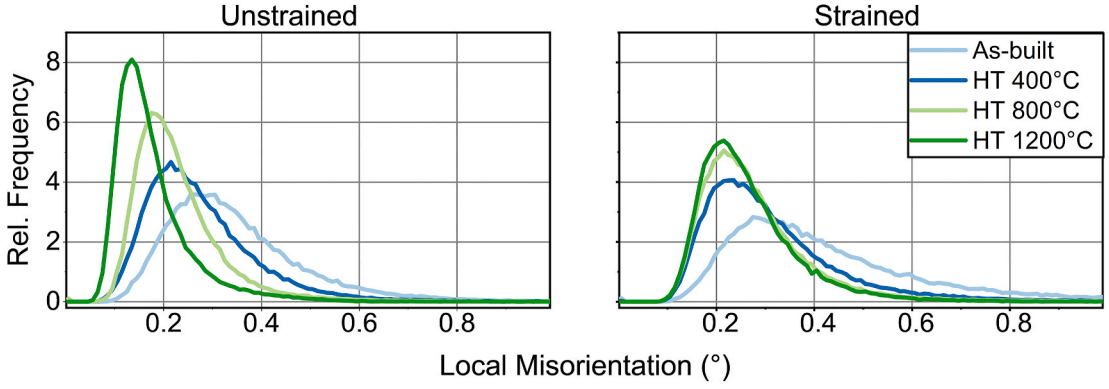

Fig. 9. Histogram of the relative frequency of local misorientations of unstrained (left) and strained (right) samples.

Table 5
The full width at half maximum of the distribution of misorientation.

Sample	Unstrained	Strained
As-built	0.25	0.31
Heat-treated at 400 °C	0.19	0.21
Heat-treated at 800 °C	0.14	0.17
Heat-treated at 1200 °C	0.10	0.16

Table 6
Cell size with 95% confidence interval measurements after pre-straining (measured on cross sections perpendicular to the building direction).

Sample	Average cell size
As-built	0.41 ± 0.05 μm
Heat-treated at 400 °C	0.44 ± 0.02 μm

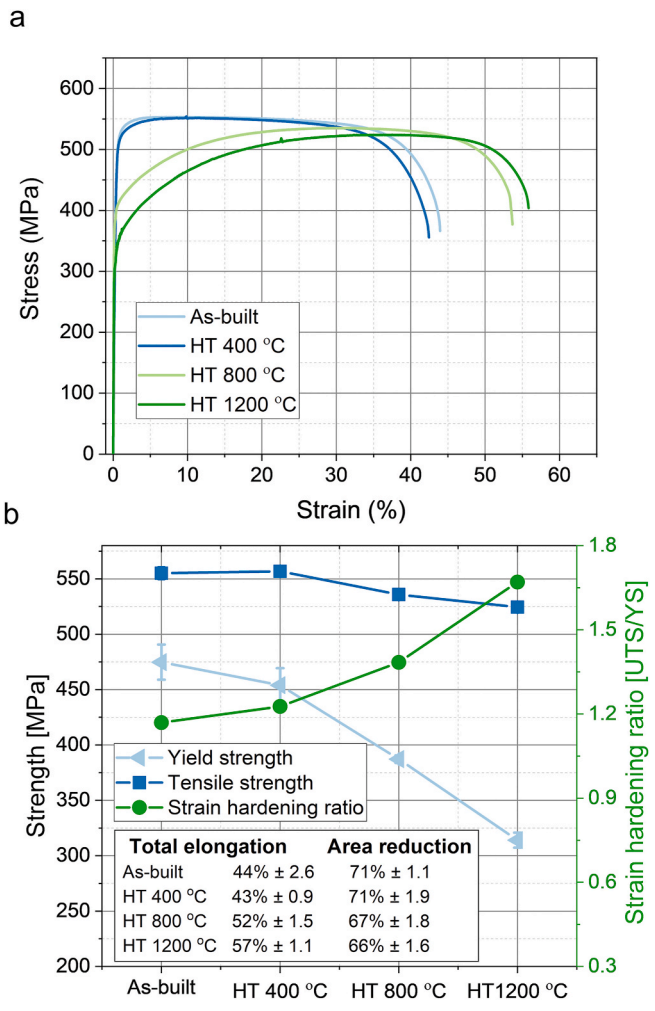

Fig. 10. (a) Representative stress/strain curves and (b) average tensile properties for the studied samples in the different conditions.

yield and tensile strength was observed; however, there was an increase in the ductility.

Surprisingly, when measuring the area reduction at the fracture surface (see Fig. 10b), it was found that all conditions exhibited similar levels of ductility. This tendency was even slightly greater in the as-built samples and the samples heat-treated at 400 °C. The reason these conditions exhibited the lowest total elongation is the relatively low strain-hardening rate ($d\sigma/d\varepsilon$), resulting in early localization of strains in a narrow necking region. Materials with higher strain-hardening ratios and more stable strain-hardening rates can counteract localized straining at the neck by extending the neck region along the straining direction, hence leading to higher total elongation. This strain-hardening ability of samples heat-treated at 800 and 1200 °C, yields distribution of strains in a wider neck and a considerably larger elongation at fracture despite the slightly lower area reduction.

Processing 316L using conventional methods creates a product with a low yield strength, but a strong strain-hardening ability. The strong strain-hardening ability generates a relativity high ultimate tensile strength (UTS). However, as-built L-PBF samples exhibit both high yield strength and UTS yet have a low strain-hardening ability, resulting in roughly the same UTS value as the cold-rolled sample. Hence, as-built L-PBF-produced components will possess a low strain-hardening ability compared with components that have been processed using conventional methods. As described above, the strain-hardening ability becomes much stronger after heat treatment at 800 and 1200 °C. Properties thus become more similar to what results from conventional processing.

4. Discussion

The intent of this study has been to investigate the role of the cell structure in L-PBF-processed 316L on material strengthening and how the strain partitioning and dislocation movement changes as this structure is annealed. The approach has been to utilize EBSD, specifically KAM maps, to study the misorientation development between cells and their corresponding boundaries as the material is strained to 20%.

The microstructural investigations of the samples revealed a commonly described elongated grain morphology with a strong <101> texturing and a cell structure that aligns itself along the direction of the heat flux [14]. The strong texturing was found to be unaffected by heat treatments in this study, which Voisin et al. also reported [24]. However, the 1200 °C heat treatment resulted in a partial recrystallization with an associated grain growth. For full recrystallization, longer holding times at this temperature would have been required [27]. It is worth mentioning that recrystallization of cold-rolled 316L occurs at the relatively lower temperature of 550 °C [28]. Hence, one can hypothesize that samples produced with L-PBF are more stable at higher temperatures and resist recrystallization. One can connect this to the fact that induced plastic strain during L-PBF processing is not significant enough to energetically favor recrystallization. Research conducted on recrystallization of cast and subsequently compressed 316L showed that cast structures recrystallize with a rate order that is magnitudes slower than when the cast material was compressed [29,30]. It is, however, difficult to delineate the cause for the sluggish recrystallization response without further experiments.

The cell size was found to be constant up until temperatures of 400 °C. However, it appeared that the cell size remained constant even after annealing at 800 °C. This was, however, not reflected in the conducted measurements due to the partial dissolution of the cell boundaries. The cells are a result of a combination of large temperature gradients and high solidification rates, where segregated alloying elements and dislocations accumulate at the cell boundaries [9–11,17,18,24]. Hence, growth of the cells is not expected as this structure is likely to merely anneal out at higher temperatures, which was observed after annealing at 1200 °C. Similar observations have been discussed by Saeidi et al. [31].

At 800 °C, the cell boundaries become much more diffuse compared to the structures observed in the as-built and annealed at 400 °C conditions. From the KAM maps in Fig. 8, one can see that the misorientation between cell interiors and cell walls were no longer present after annealing at 800 °C, and the misorientation could only be detected at the grain boundaries. Fig. 9 also confirms these findings, as the distribution of the misorientation shifts toward lower degrees while also

becoming narrower – this is indicative of a lattice relatively free from plastic strain [32,33]. It seems that the dislocation network is more easily annealed out compared to the elements that have segregated to the cell boundaries.

However, investigations of thin foil samples revealed that after the heat treatment at 800 °C, both the Cr and Mo segregation and the thick dislocation tangles had homogenized and annealed out relative to the as-built state. It is, however, possible that there might be a residual segregation of elements that was not revealed by the measurements. Birnbaum et al. [18] offer another explanation; the highly defective structure of L-PBF-processed material provides enhanced diffusion paths that, together with the associated length scales, enables homogenization of Cr and Mo even at relatively low temperatures. Voisin et al.'s [24] findings confirm the rapid homogenization of Cr and Mo, where only minor enrichments (below 0.5 at.%) of Cr were found after similar heat treatments at 800 °C. Further evidence that dislocation annihilation is activated at lower temperatures can be found through a comparison of the as-built and the 400 °C samples. Here, a noticeable shift in the misorientation distribution to lower angles was observed, signifying a lower amount of strain. Since an increased dislocation density increases the tensile strength [9,13,15] by reducing the dislocation density through heat treatment, there will be a reduction of the tensile strength as shown in Fig. 10.

After applying a strain of 20%, a greater strain accumulation was found in the cell boundaries of the as-built samples and samples annealed at 400 and 800 °C as compared to their unstrained counterparts (Fig. 8). The absence of a peak shift in the as-built condition indicates that the unstrained sample was already saturated in dislocations. Liu et al. [34] report this sort of strain accumulation, which they explained by a momentarily pile-up of dislocations at the cell boundaries as slip systems become active and dislocations begin to mobilize. The same study shows that cell walls only act as movement moderators, allowing for some dislocation slip between cells, hence increasing the ductility of L-PBF-processed 316L. Interestingly, an increased strain accumulation at the cell boundaries was also observed in the sample heat-treated at 800 °C, where no significant accumulation was observed in the unstrained sample. Hence, despite elemental homogenization within the cell walls and the reduction in the dislocation density, the strain re-accumulates at the cell walls. This indicates that when coupled with diminishing elemental segregation in the cell walls, even relatively low densities of dislocations can provide a dislocation pinning effect.

Without more advanced analytical work, it is difficult to explain the mechanism behind this. However, existing research on the matter provides possible explanations. Studies have shown that the dislocation tangles at cell walls dissociate into Shockley partials that form immobile stacking faults, hence providing a Lomer-Cottrell-type junction [24]. Such immobile dislocations provide strong resistance to gliding dislocations [35] and can therefore cause re-accumulation of strain at the cell walls. That phenomenon would explain the results of the pre-strained sample that had been annealed at 800 °C, as immobile dislocations are not easily annealed out. With that said, the pre-existence of a dislocation network strongly affects the yielding point. This increases the critical shear stress necessary to initiate dislocation movement. These observations also explain the difference in the tensile properties between the samples heat-treated at 800 °C and 1200 °C; the 1200 °C annealed sample had a considerably lower yield strength. It is also worth mentioning that the melt pool boundaries did not accumulate any strain and should not therefore have any major contribution to the tensile properties. The minor difference in yield strength between the as-built and samples heat-treated at 400 °C is somewhat expected, as no differences in the cellular structure were observed between the samples.

In addition, the cells were found to be relativity stable during the deformation and remained unchanged in shape and size at 20% strain. This might seem counter intuitive. However, it can be explained by the deformation behavior of austenitic stainless steels, which occurs through combined slip and twinning mechanisms [9,13,34]. Thus, the strain accommodation occurs through twin bundles that propagate through both cells and low angle grain boundaries [9,34] and not solely through the cells. Therefore, when strained, the cells do not strictly elongate along the loading direction.

Despite the general similarities in the microstructures of the samples annealed at 400 and 800 °C, there was a considerable difference in the strain-hardening ratio during the tensile testing. This indicates that the cells and the associated dislocations are a major factor for a low yet steady level of strain-hardening behavior, which was discussed earlier with regards to the findings of the KAM maps. Additionally, the complete dissolution of both the dislocation and cell boundary structure resulted in the deterioration of the mechanical properties, as seen in the 1200 °C-annealed sample. While the as-built and heat-treated at 400 °C samples provide both high yield strength and good ductility on the local scale, the ability to strain harden is rather limited. The strain-hardening ratio has important engineering implications as it allows the material to absorb more strain before failing; this is useful in, for example, metal shaping operations and designing safety margins in components. While metal shaping is perhaps not relevant in the case of L-PBF-built components, the safety margins for design still must be respected. Therefore, from an engineering design perspective, the finding that the materials treated at moderate temperatures (between 400 and 800 °C) yielded higher strain-hardening ratios might make this temperature treatment a more suitable choice for most applications.

5. Summary and conclusions

This study investigated the microstructure and tensile properties of 316L stainless steel produced by L-PBF in as-built and heat-treated states in both unstrained and strained to 20% conditions. The aim was to evaluate strain accumulation in the cell boundaries as a function of annealing temperatures ranging from 400 °C to 1200 °C. One can draw the following conclusions from the results of this study:

- A strong <101> texture along the building direction is maintained up to 1200 °C, while the cell structure is completely dissolved. At 800 °C, the cell boundaries become more ambiguous (although are still visible) compared to the as-built and 400 °C conditions.
- The dislocation network exists concurrently with elemental segregation of Mo and Cr at the cell walls in as-built and 400 °C heat-treated samples.
- Heat-treating the samples at 1200 °C resulted in a 50% drop in yield strength compared to the as-built sample (475 MPa to 314 MPa), whereas a heat treatment at 400 °C did not have a significant effect on the samples' tensile properties. The complete disappearance of both the dislocation and cell boundary structure resulted in a strong reduction in the yield stress, as seen in the 1200 °C annealed samples.
- The as-built and heat-treated at 400 °C samples presented a significant strain accumulation at the cell boundaries in the unstrained state. However, no strain accumulation was observed at the cell boundaries of the sample heat-treated at 800 °C.
- After applying a strain of 20%, an increased strain accumulation was found in the cell boundaries of the as-built samples and samples annealed at 400 and 800 °C as compared to their unstrained counterparts. This indicates that the cell boundaries provide a dislocation pinning effect.
- The strain accumulation at the cell boundaries of the strained samples that were heat-treated at 800 °C indicates that even a minor presence of dislocation tangles can provide a dislocation pinning effect. This suggests that the cell walls contain some dislocations that are more difficult to anneal, possibly of an immobile character. Hence, both the dislocation network and the segregated elements act to store and slow down dislocations and their movement as the material plastically deforms.

CRediT authorship contribution statement

D. Riabov: Conceptualization, Investigation, Visualization, Validation, Writing – original draft. **A. Leicht:** Conceptualization, Investigation, Visualization, Validation, Writing – original draft. **J. Ahlström:** Writing – review & editing. **E. Hryha:** Supervision, Writing – review & editing.

Declaration of competing interest

The authors declare that they have no known competing financial interests or personal relationships that could have appeared to influence the work reported in this paper.

Acknowledgments

This research was carried out in the Centre for Additive Manufacturing – Metal (CAM^2) as part of a joint project financed by Swedish Governmental Agency of Innovation Systems (Vinnova), coordinated by Chalmers University of Technology. The work was performed in part at the Chalmers Materials Analysis Laboratory CMAL.

Appendix A. Supplementary data

Supplementary data to this article can be found online at https://doi.org/10.1016/j.msea.2021.141699.

Data availability

The raw/processed data that support the findings of this paper are available from the authors on reasonable request.

References

[1] C.C. Koch, Optimization of strength and ductility in nanocrystalline and ultrafine grained metals, Scripta Mater. 49 (2003) 657–662, https://doi.org/10.1016/S1359-6462(03)00394-4.
[2] D.G. Morris, Mechanical Behaviour of Nanostructured Materials, Trans Tech Publ, n.d.
[3] R.Z. Valiev, I. V Alexandrov, Y.T. Zhu, T.C. Lowe, Paradox of strength and ductility in metals processed Bysevere plastic deformation, J. Mater. Res. 17 (2002) 5–8, https://doi.org/10.1557/JMR.2002.0002.
[4] Y. Wang, M. Chen, F. Zhou, E. Ma, High tensile ductility in a nanostructured metal, Nature 419 (6910) (2002) 912–915, https://doi.org/10.1038/nature01133.
[5] R.Z. Valiev, A.V. Sergueeva, A.K. Mukherjee, The effect of annealing on tensile deformation behavior of nanostructured SPD titanium, Scripta Mater. 49 (2003) 669–674, https://doi.org/10.1016/S1359-6462(03)00395-6.
[6] M.A. Meyers, A. Mishra, D.J. Benson, Mechanical properties of nanocrystalline materials, Prog. Mater. Sci. 51 (2006) 427–556, https://doi.org/10.1016/j.pmatsci.2005.08.003.
[7] F.K. Yan, G.Z. Liu, N.R. Tao, K. Lu, Strength and ductility of 316L austenitic stainless steel strengthened by nano-scale twin bundles, Acta Mater. 60 (2012) 1059–1071, https://doi.org/10.1016/j.actamat.2011.11.009.
[8] X. Wu, M. Yang, F. Yuan, G. Wu, Y. Wei, X. Huang, Y. Zhu, Heterogeneous lamella structure unites ultrafine-grain strength with coarse-grain ductility, Proc. Natl. Acad. Sci. U. S. A 112 (2015) 14501–14505, https://doi.org/10.1073/pnas.1517193112.
[9] Y.M. Wang, T. Voisin, J.T. McKeown, J. Ye, N.P. Calta, Z. Li, Z. Zeng, Y. Zhang, W. Chen, T.T. Roehling, R.T. Ott, M.K. Santala, P.J.J.J. Depond, M.J. Matthews, A. V. Hamza, T. Zhu, Additively manufactured hierarchical stainless steels with high strength and ductility, Nat. Mater. 17 (2018) 63–70, https://doi.org/10.1038/NMAT5021.
[10] K. Saeidi, X. Gao, Y. Zhong, Z.J.J. Shen, Hardened austenite steel with columnar sub-grain structure formed by laser melting, Mater. Sci. Eng. 625 (2015) 221–229, https://doi.org/10.1016/j.msea.2014.12.018.
[11] L. Liu, Q. Ding, Y. Zhong, J. Zou, J. Wu, Y.L. Chiu, J. Li, Z. Zhang, Q. Yu, Z. Shen, Dislocation network in additive manufactured steel breaks strength–ductility trade-off, Mater. Today 21 (2018) 354–361, https://doi.org/10.1016/j.mattod.2017.11.004.
[12] X. Wang, J.A. Muñiz-Lerma, O. Sánchez-Mata, M. Attarian Shandiz, M. Brochu, Microstructure and mechanical properties of stainless steel 316L vertical struts manufactured by laser powder bed fusion process, Mater. Sci. Eng. 736 (2018) 27–40, https://doi.org/10.1016/j.msea.2018.08.069.
[13] M.S. Pham, B. Dovgyy, P.A. Hooper, Twinning induced plasticity in austenitic stainless steel 316L made by additive manufacturing, Mater. Sci. Eng. 704 (2017) 102–111, https://doi.org/10.1016/j.msea.2017.07.082.
[14] D. Wang, C. Song, Y. Yang, Y. Bai, Investigation of crystal growth mechanism during selective laser melting and mechanical property characterization of 316L stainless steel parts, Mater. Des. 100 (2016) 291–299, https://doi.org/10.1016/j.matdes.2016.03.111.
[15] Y. Zhong, L. Liu, S. Wikman, D. Cui, Z. Shen, Intragranular cellular segregation network structure strengthening 316L stainless steel prepared by selective laser melting, J. Nucl. Mater. 470 (2016) 170–178, https://doi.org/10.1016/j.jnucmat.2015.12.034.
[16] K. Saeidi, X. Gao, F. Lofaj, L. Kvetková, Z.J.J. Shen, Transformation of austenite to duplex austenite-ferrite assembly in annealed stainless steel 316L consolidated by laser melting, J. Alloys Compd. 633 (2015) 463–469, https://doi.org/10.1016/j.jallcom.2015.01.249.
[17] K.M. Bertsch, G. Meric de Bellefon, B. Kuehl, D.J. Thoma, Origin of dislocation structures in an additively manufactured austenitic stainless steel 316L, Acta Mater. 199 (2020) 19–33, https://doi.org/10.1016/j.actamat.2020.07.063.
[18] A.J. Birnbaum, J.C. Steuben, E.J. Barrick, A.P. Iliopoulos, J.G. Michopoulos, Intrinsic strain aging, Σ3 boundaries, and origins of cellular substructure in additively manufactured 316L, Additive Manufacturing 29 (2019), 100784, https://doi.org/10.1016/j.addma.2019.100784.
[19] G. Wang, H. Ouyang, C. Fan, Q. Guo, Z. Li, W. Yan, Z. Li, The origin of high-density dislocations in additively manufactured metals, Materials Research Letters 8 (2020) 283–290, https://doi.org/10.1080/21663831.2020.1751739.
[20] O.O. Salman, C. Gammer, A.K. Chaubey, J. Eckert, S. Scudino, Effect of heat treatment on microstructure and mechanical properties of 316L steel synthesized by selective laser melting, Mater. Sci. Eng. 748 (2019) 205–212, https://doi.org/10.1016/j.msea.2019.01.110.
[21] M.S.I.N. Kamariah, W.S.W. Harun, N.Z. Khalil, F. Ahmad, M.H. Ismail, S. Sharif, Effect of heat treatment on mechanical properties and microstructure of selective laser melting 316L stainless steel, IOP Conf. Ser. Mater. Sci. Eng. 257 (2017), https://doi.org/10.1088/1757-899X/257/1/012021.
[22] D. Riabov, M. Rashidi, E. Hryha, S. Bengtsson, Effect of the powder feedstock on the oxide dispersion strengthening of 316L stainless steel produced by laser powder bed fusion, Mater. Char. 169 (2020), 110582, https://doi.org/10.1016/j.matchar.2020.110582.
[23] L. Cui, S. Jiang, J. Xu, R.L. Peng, R.T. Mousavian, J. Moverare, Revealing relationships between microstructure and hardening nature of additively manufactured 316L stainless steel, Mater. Des. 198 (2021), 109385, https://doi.org/10.1016/j.matdes.2020.109385.
[24] T. Voisin, J.-B. Forien, A. Perron, S. Aubry, N. Bertin, A. Samanta, A. Baker, Y. M. Wang, New insights on cellular structures strengthening mechanisms and thermal stability of an austenitic stainless steel fabricated by laser powder-bed-fusion, Acta Mater. 203 (2021), 116476, https://doi.org/10.1016/j.actamat.2020.11.018.
[25] C. Pauzon, E. Hryha, P. Forêt, L. Nyborg, Effect of argon and nitrogen atmospheres on the properties of stainless steel 316 L parts produced by laser-powder bed fusion, Mater. Des. 179 (2019), 107873, https://doi.org/10.1016/j.matdes.2019.107873.
[26] M.P. Haines, N.J. Peter, S.S. Babu, E.A. Jägle, In-situ Synthesis of Oxides by Reactive Process Atmospheres during L-PBF of Stainless Steel, Additive Manufacturing, 2020, 101178, https://doi.org/10.1016/j.addma.2020.101178.
[27] D. Kong, C. Dong, X. Ni, L. Zhang, J. Yao, C. Man, X. Cheng, K. Xiao, X. Li, Mechanical properties and corrosion behavior of selective laser melted 316L stainless steel after different heat treatment processes, J. Mater. Sci. Technol. 35 (2019) 1499–1507, https://doi.org/10.1016/j.jmst.2019.03.003.
[28] C. Herrera, R.L. Plaut, A.F. Padilha, Microstructural refinement during annealing of plastically deformed austenitic stainless steels, Mater. Sci. Forum (2007) 423–428.
[29] M.C. Mataya, E.R. Nilsson, E.L. Brown, G. Krauss, Hot working and recrystallization of As-Cast 316L, Metall. Mater. Trans. 34 (2003) 1683–1703, https://doi.org/10.1007/s11661-003-0313-8.
[30] G.T. Campbell, E.P. Abrahamson, N.J. Grant, The recrystallization behavior of an austenitic stainless steel Ingot structure due to hot deformation, Metall Trans 5 (1974) 1875–1881, https://doi.org/10.1007/BF02644154.
[31] K. Saeidi, F. Akhtar, Subgrain-controlled grain growth in the laser-melted 316 L promoting strength at high temperatures, Royal Society Open Science 5 (2018), https://doi.org/10.1098/rsos.172394.
[32] S.I. Wright, M.M. Nowell, D.P. Field, A review of strain analysis using electron backscatter diffraction, Microsc. Microanal. 17 (2011) 316–329, https://doi.org/10.1017/S1431927611000055.
[33] S. Sinha, J.A. Szpunar, N.A.P. Kiran Kumar, N.P. Gurao, Tensile deformation of 316L austenitic stainless steel using in-situ electron backscatter diffraction and crystal plasticity simulations, Mater. Sci. Eng. 637 (2015) 48–55, https://doi.org/10.1016/j.msea.2015.04.005.
[34] L. Liu, Q. Ding, Y. Zhong, J. Zou, J. Wu, Y.L. Chiu, J. Li, Z. Zhang, Q. Yu, Z. Shen, Dislocation network in additive manufactured steel breaks strength–ductility trade-off, Mater. Today 21 (2018) 354–361, https://doi.org/10.1016/j.mattod.2017.11.004.
[35] D. Hull, D.J. Bacon, Introduction to Dislocations, Elsevier, 2011.